MATERIALS CHEMISTRY
FRONTIERS

RESEARCH ARTICLE

View Article Online
View Journal | View Issue

Cite this: *Mater. Chem. Front.*, 2023, **7**, 4132

Universal synthesis of rare earth-doped FeP nanorod arrays for the hydrogen evolution reaction†

Minnan Chen, Zijing Lin, Yi Ren, Xuan Wang, Meng Li, Dongmei Sun, * Yawen Tang * and Gengtao Fu *

Received 5th May 2023,
Accepted 6th July 2023

DOI: 10.1039/d3qm00516j

rsc.li/frontiers-materials

A universal plasma-assisted strategy is proposed for the fabrication of rare earth (RE)-doped FeP nanorod arrays (RE-FeP) as a kind of potential electrocatalyst for the hydrogen evolution reaction (HER). The energetic Ar plasma can induce the vacancy-enriched feature of the Fe-precursor, which assists in the anchoring of RE ions. As a typical model, Sm-FeP affords a low overpotential of 71 mV at 10 mA cm^{-2} for the HER, which is 63 mV smaller than that of FeP and superior to most reported Fe-based catalysts. The robust long-term stability of Sm-FeP is also demonstrated. Furthermore, the as-assembled Sm-FeP‖RuO_2 water-splitting electrolyzer also displays a low cell voltage of 1.59 V at 10 mA cm^{-2}. Sm-induced electronic configuration modulation at the Fe site mainly contributes to the improved HER performance of Sm-FeP relative to FeP. The combination between the Sm site and *OH produces labile O 2p states below the Fermi level, thus weakening the co-adsorption of *OH and *H derived from the splitting of H_2O for the facilitated formation of *H. Moreover, the other RE-FeP catalysts (*e.g.*, Yb, Eu, La, and Er) extended by such a plasma-induced strategy also exhibit various improved degrees in the HER, implying that RE-FeP is a promising class of electrocatalyst towards the HER.

Introduction

Hydrogen (H_2) has attracted great attention as a clean and renewable alternative energy source for traditional fossil fuels due to its zero-carbon emission and high gravimetric energy density (142 MJ kg^{-1}).[1,2] The electrocatalytic water splitting is deemed as an environment-friendly strategy to meet the rising demands of high-purity hydrogen production.[3,4] However, the efficiency of water splitting is mainly decided by the electrocatalytic performance of catalysts to lower the energy barrier of the involved reactions such as the hydrogen evolution reaction (HER).[5–8] To date, Pt-based materials are still considered the benchmark HER electrocatalyst,[9–12] but high-cost and limited reserves hinder their large-scale application. Therefore, it is highly desirable to develop earth-abundant, cost-effective, and efficient non-Pt catalysts for the HER.[13,14]

Recently, a myriad of 3d-transition metal (TM)-based catalysts, such as alloys,[15,16] hydroxides,[17,18] nitrides,[19,20] oxides,[21,22] sulfides,[23,24] and phosphides,[25,26] have been developed to accelerate the HER process. Thereinto, FeP has been identified as one of the prospective HER catalysts owing to its unique proton attractivity.[27,28] Meanwhile, P element with slightly high electronegativity compared with Fe can regulate the surface charge state of Fe and also increase the stability of FeP through a covalent Fe–P bond.[29] However, there is still a huge performance gap between FeP and Pt-based catalysts and bulk FeP cannot provide sufficient exposed active sites and mass transfer channels for the HER, which is far from the demand of renewable energy systems. To address the above-mentioned problems, incorporation of FeP with heteroatoms seems to be a reliable strategy to improve the HER activity. Owing to the extensibility of the electron wave function of d orbitals, the electronic structure of Fe can be finely adjusted by foreign elements, which affects the adsorption behaviors of the reaction intermediates in the HER.[30–32]

More recently, rare earth (RE) elements such as La, Ce, Nb, Eu, Gd, and Yb have been proven as efficient promoters for a number of electrocatalytic reactions.[33–40] The unique 4f-subshell electron configuration, flexible valence states, and strong spin–orbital effect of RE elements can offer great potential for tuning the electronic structures and improving the electrocatalytic performance of various TM-based

Jiangsu Key Laboratory of New Power Batteries, Jiangsu Collaborative Innovation Center of Biomedical Functional Materials, School of Chemistry and Materials Science, Nanjing Normal University, Nanjing 210023, China.
E-mail: sundongmei@njnu.edu.cn, tangyawen@njnu.edu.cn, gengtaofu@njnu.edu.cn

† Electronic supplementary information (ESI) available. See DOI: https://doi.org/10.1039/d3qm00516j

catalysts.[41–44] For example, Sun *et al.* found that the combination of Yb_2O_3 and Ni can reduce the energy barrier of water dissociation and enlarge the active-site density, which greatly enhances the HER performance of Ni.[45] Li *et al.* demonstrated that the co-doping of Y and Ce into Ni-MOF can finely tailor the electronic structure of NiYCe-MOF/NF by a bimetallic synergistic effect, resulting in greatly enhanced HER and OER performance.[46] However, compared with Fe, RE elements have a larger atomic radius, more negative reduction potential, and stronger oxygen affinity, which increase the difficulty of controllable synthesis of RE-FeP hybrid catalysts. According to defect theory, the unsaturated properties of atoms around defect sites tend to possess high binding energy with metal ions, which can act as anchoring sites for foreign atoms or clusters. This vacancy-assisted anchoring method can effectively avoid self-nucleation of heterogeneous elements due to crystal nucleation and differences in growth factors of different elements (*e.g.*, atomic radius, charge, and solubility). For example, Gong *et al.* reported that O-doped MoS_2 could generate rich sulfur vacancies that provide specific anchoring sites for Pt and facilitate the formation of homogeneous and monodispersed Pt nanoparticles.[47] Wang *et al.* also reported that Au atoms were captured by oxygen vacancy-enriched TiO_2 with the local atomic configuration of Ti–Au–Ti by a coprecipitation method.[48] Therefore, the hybridization of FeP and RE species through the vacancy-assisted method may be a viable strategy to improve the HER activity of FeP.

Herein, we elaborate on a universal plasma-assisted strategy for the synthesis of RE-FeP nanorod arrays on carbon cloth (RE-FeP@CC) as highly efficient HER catalysts. The Ar-plasma beam sheds the surface light atoms of the FeO(OH)@CC precursor to form vacancies, so as to anchor glycine-stabilized RE ions during the subsequent hydrothermal process. Taking Sm-FeP@CC as an example, Sm-FeP@CC exhibits outstanding electrocatalytic activity with a low overpotential of 71 mV at 10 mA cm^{-2}, a small Tafel slope of 85.9 mV dec^{-1}, and robust stability, outperforming those of Sm-free FeP@CC and most reported Fe-based catalysts. When utilized in overall water splitting, Sm-FeP@CC‖RuO_2 only requires a voltage of 1.59 V at 10 mA cm^{-2}. The improved HER activity of Sm-FeP@CC is highly correlated with the Sm-induced electronic modulation of Fe and the unique nanorod arrayed feature. Theoretical calculations demonstrate that the increased HER performance on Sm-FeP is due to the weakened co-adsorption of *OH and *H that is contributed by the splitting of H_2O, where the labile O 2p state in *OH denotes the weak bonding at the Sm site, which is favored for the consecutive H_2 release.

Results and discussion

Synthesis and characterization

Sm-FeP@CC was synthesized by the combination of an Ar-plasma-assisted treatment and subsequent topological transformation with FeO(OH) as the precursor, as

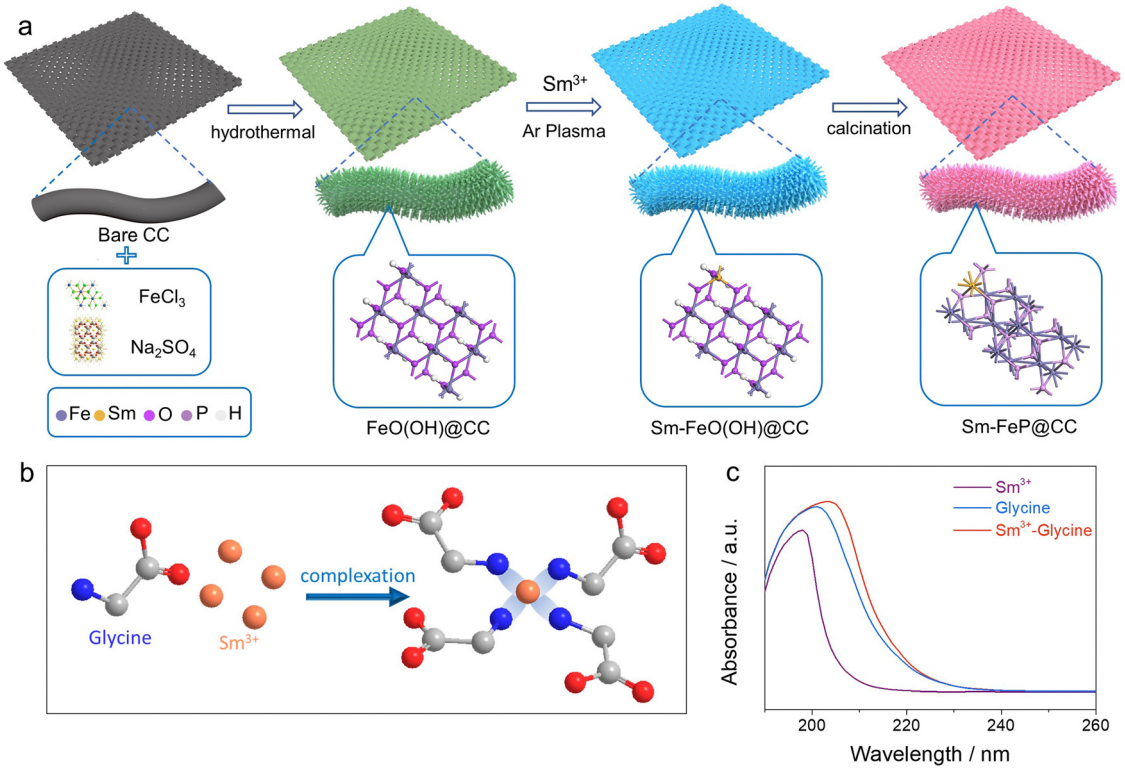

Fig. 1 (a) A schematic of the fabrication procedure of Sm-FeP@CC; (b) a schematic of the interaction between Sm^{3+} and glycine; (c) UV-vis absorption spectra of Sm^{3+}, glycine, and Sm^{3+}–glycine aqueous solution.

schematically illustrated in Fig. 1(a). Firstly, the FeO(OH) nanorod arrays were uniformly grown on the carbon cloth (CC) substrate through a simple hydrothermal process. Then, the FeO(OH)@CC was treated with Ar plasma for obtaining anionic vacancies on its surface, which was further soaked in $SmCl_3$ glycine solution. Glycine not only can be adsorbed by anionic vacancies through electrostatic interactions but also can coordinate with the Sm^{3+} (Fig. 1(b)). UV-vis spectra illustrated that Sm^{3+}–glycine solution has a distinct red shift compared to $SmCl_3$ solution (Fig. 1(c)), indicating that the Sm^{3+} ion was coordinated with glycine. Finally, Sm-modified FeO(OH)@CC was topologically transferred into Sm-FeP@CC by the phosphating process.

The crystalline structure of Sm-FeP@CC was analyzed by X-ray powder diffraction (XRD), as shown in Fig. 2(a). The characteristic diffraction peaks for FeP were observed at 32.7°, 37.1° and 48.3°, which are well indexed to (011), (111), and (211) facets of orthorhombic-phase FeP (JCPDF no. 65-2595), demonstrating that the introduction of Sm element does not change the host crystalline structure of FeP. Two obvious diffraction peaks of about 26.5° and 44.0° correspond to the lattice planes of carbon cloth. The magnified (211) facet peak of Sm-FeP shows an obvious shift to a lower angle region compared with FeP (Fig. S1, ESI†), which can be ascribed to the lattice expansion due to the lager atomic radius of Sm. Sm-FeP@CC was converted from the orthorhombic FeO(OH) phase (Fig. S2, ESI†). The existence of Sm in Sm-FeP@CC was also confirmed by the energy dispersive spectroscopy (EDS) spectrum (Fig. S3, ESI†). The molar content of Sm in Sm-FeP was calculated to be about 1.37% by inductively coupled plasma mass spectrometry (ICP-MS). The surface composition and valence information of Sm-FeP@CC were further investigated by X-ray photoelectron spectroscopy (XPS). The coexistence of Fe, P, Sm and C was clearly observed in the survey scan spectrum for Sm-FeP@CC (Fig. S4, ESI†), consistent with the analysis of EDS. The Sm 3d peaks of Sm 3d5/2 and Sm 3d3/2 were found at two distinct binding energies of 1083.3 and 1110.5 eV (Fig. 2(b)). The binding energy difference between the two spin–orbit peaks is about 27.2 eV, indicating that Sm presents the +3 oxidation state in the host.[49] For the high-resolution Fe 2p spectrum (Fig. 2(c)), the deconvoluted peaks located at 711.1 and 724.3 eV are ascribed to Fe^{2+} species, while the deconvoluted peaks at 713.7 and 727.1 eV are assigned to Fe^{3+} species with two satellite peaks.[50,51] Besides, a pair of sharp peaks represented at 720.2 and 707.6 eV are ascribed to FeP.[52–54] The binding energy of the Fe 2p3/2 peak for Sm-FeP@CC shifts to a lower position by about 0.3 eV compared with FeP@CC (Fig. 2(c)), while a significant positive shift of about 0.50 eV of Sm 3d5/2 was also observed in Sm-FeP@CC compared to Sm_2O_3 (Fig. S5, ESI†). This indicates that the introduction of Sm optimizes the electronic structure of FeP owing to the different electronegativities of Sm and Fe.[53,55] Such spontaneous electron migration can equilibrate the adsorption energies of intermediates and improve the hydrogen evolution performance.[56–58] The high-resolution P 2p spectrum (Fig. 2(d)) of Sm-FeP@CC is disassembled into one peak of P–O at 133.9 eV originating from surface oxidation of the phosphides and other peaks centered at 129.5 eV and 130.3 eV belong to P 2p3/2 and P 2p1/2 peaks of the P-metal bond.[59,60] The strong P–O bond can be ascribed to both surface oxidation caused by exposure to air and the deposition of PO_3^{3-} species due to the decomposition of sodium hypophosphite.[61] After Sm doping, the Sm-FeP@CC exhibits a higher electron spin response (ESR) signal intensity at a g value of 2.004 than FeP@CC (Fig. 2(e)), which implies the presence of high concentration P vacancies in Sm-FeP@CC. Sm with a flexible 4f-subshell electron configuration

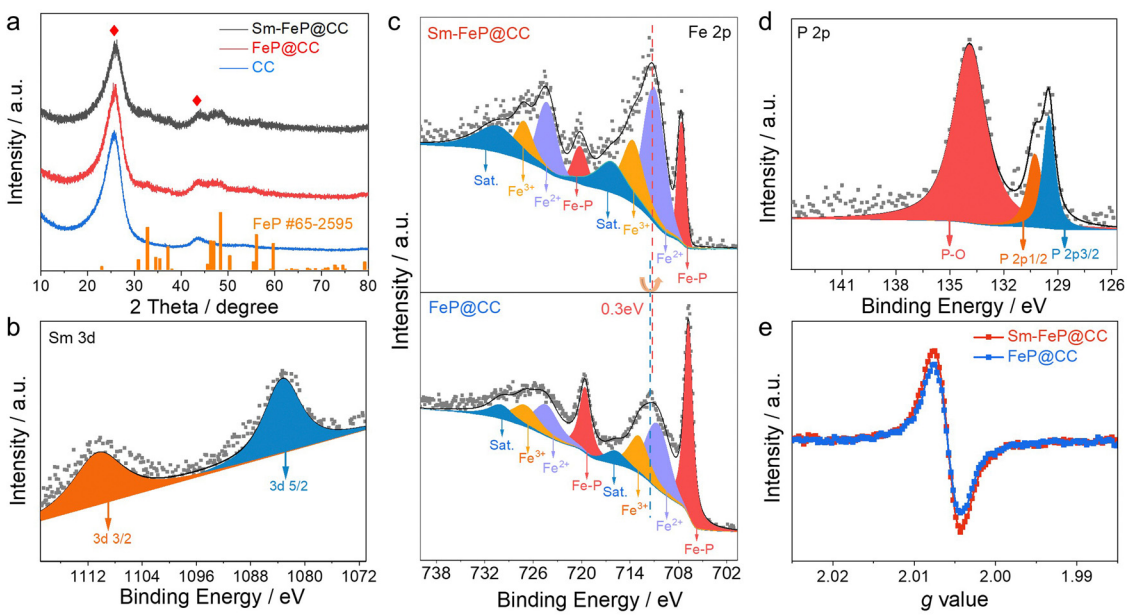

Fig. 2 (a) XRD pattern of Sm-FeP@CC; (b) Sm 3d XPS spectrum of Sm-FeP@CC; (c) Fe 2p XPS spectra of Sm-FeP@CC and FeP@CC; (d) P 2p XPS spectrum of Sm-FeP@CC; (e) ESR spectra of Sm-FeP@CC and FeP@CC.

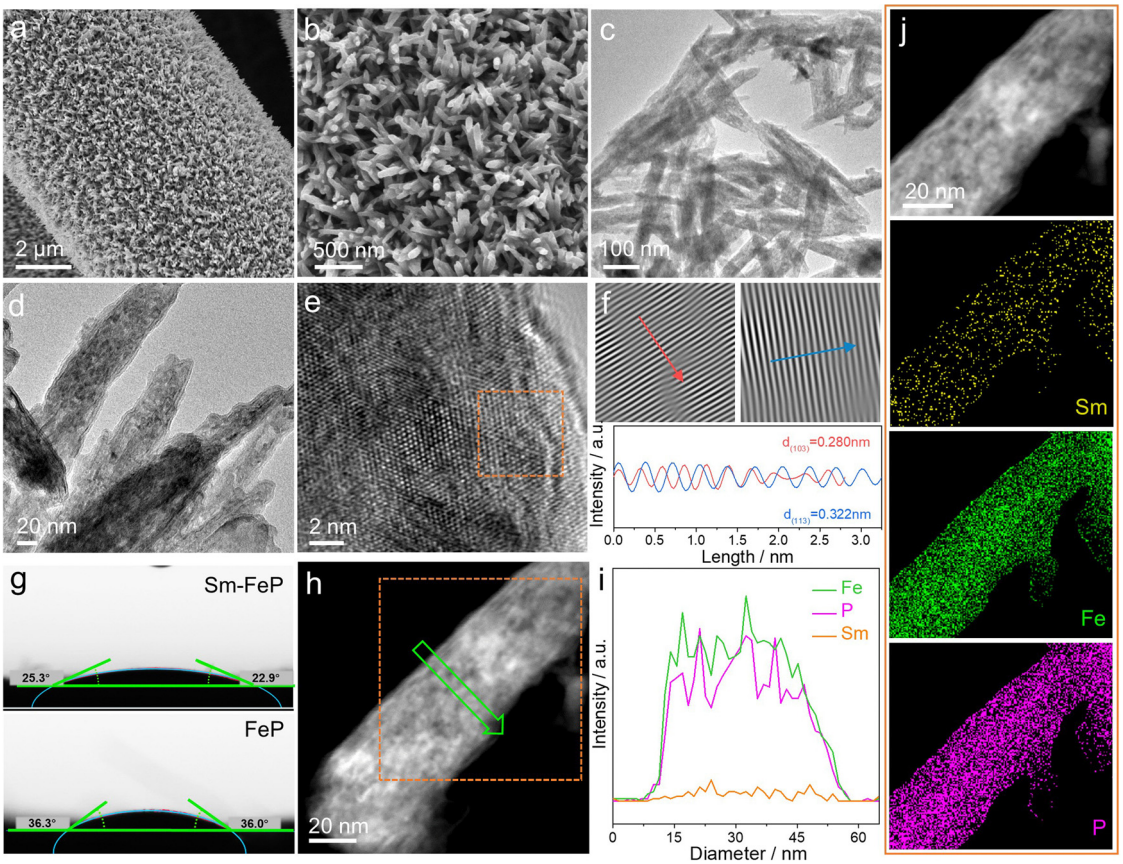

Fig. 3 Morphology and structure characterization of Sm-FeP@CC: (a), (b) SEM images; (c), (d) TEM images; (e) HRTEM image and (f) HRTEM images after noise elimination and corresponding integrated pixel intensities. (g) Contact angle with a water drop; (h) HAADF-STEM image and (i) EDS line scan profiles. (j) Elemental mapping images.

and the strong spin–orbital effect can significantly decrease the formation energy of vacancies, which may result in the vacancy-rich feature of Sm-FeP@CC.[62,63]

The morphological characteristics of the samples were characterized by scanning electron microscopy (SEM). The precursor of FeO(OH)@CC presents an array structure consisting of abundant one-dimensional (1D) nanorods on the surface of carbon cloth (Fig. S6, ESI†). After the plasma treatment and topological transformation, the Sm-FeP@CC still maintains a good rod-like array structure (Fig. 3(a)). The average length of Sm-FeP nanorods is about 160 nm and the thickness is about 50 nm (Fig. 3(b)). Likewise, FeP@CC displays a similar structure characteristic of Sm-FeP@CC (Fig. S7, ESI†), implying that Sm doping did not affect the morphology of Sm-FeP@CC. The Sm-FeP nanorods present a porous feature, as verified by transmission electron microscopy (TEM) in Fig. 3(c) and (d), which favors the exposure of more active sites. As shown in Fig. 3(f), the integrated pixel intensity derived from Fig. 3(e) shows two lattice fringe values of 0.280 nm and 0.322 nm, which are slightly larger than those of the FeP (103) and FeP (113) planes (0.276 nm and 0.320 nm). This can be attributed to the lattice expansion of FeP caused by Sm-doping. The nanoarray structure generally increases the active surface area and facilitates contact with the electrolyte,[64,65] which leads to good hydrophilicity of Sm-FeP@CC and FeP@CC with small contact angles of about 23° and 36° (Fig. 3(g)). The high-angle annular dark-field scanning TEM (HAADF-STEM) image (Fig. 3(h)) and the line scanning profiles (Fig. 3(i)) demonstrate the uniform distribution of Sm, Fe and P elements in Sm-FeP, in accordance with elemental mapping images (Fig. 3(j)).

Electrocatalytic performance for the HER

The HER performance of Sm-FeP@CC was explored by using a typical three-electrode cell in an Ar-saturated 1 M KOH solution and compared to those of FeO(OH)@CC, FeP@CC, and commercial Pt/C. Fig. 4(a) shows the linear sweep voltammetry (LSV) curves of all catalysts at a scan rate of 5 mV s^{-1}. As observed, the FeO(OH)@CC shows almost no HER activity. The Sm-FeP@CC requires an overpotential of merely 71 mV to yield the current density of 10 mA cm^{-2}, which is 63 mV more negative than that of FeP@CC (Fig. 4(b)). The overpotential of Sm-FeP@CC at a high current density of 100 mA cm^{-2} is about 175 mV, much smaller than that of FeP@CC (281 mV) and commercial Pt/C (237 mV), indicating that Sm-FeP@CC is expected to be developed for practical industrial application. The good HER performance of Sm-FeP at a high current density may have contributed to the nanorod arrayed structure and the heteroatom Sm doping, which facilitates the mass transfer

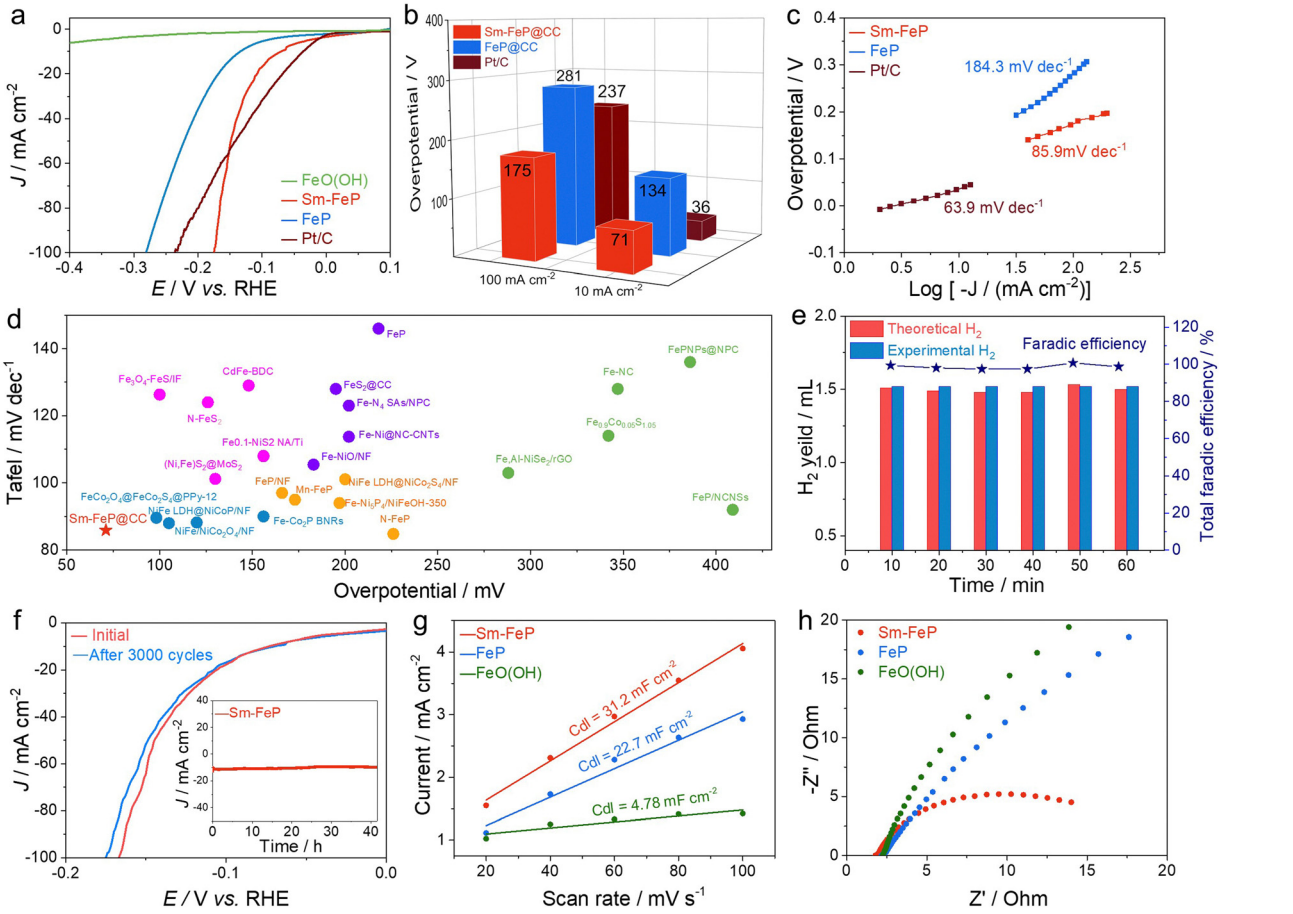

Fig. 4 Comparison of the HER activity of Sm-FeP@CC with other samples in 1 M KOH solution: (a) HER polarization curves; (b) overpotentials at 10 mA cm^{-2} and 100 mA cm^{-2}; (c) Tafel plots derived from (a); (d) HER performance comparison of Sm-FeP@CC with other recently reported Fe-based catalysts; (e) the H_2 yield and faradaic efficiency of Sm-FeP@CC for the HER; (f) HER polarization curves of Sm-FeP@CC before and after 3000 cycles of CV, where the inset shows the *i*–*t* curve of Sm-FeP@CC; (g) C_{dl} values and (h) EIS Nyquist plots of the catalysts.

process and charge-transfer rate between the electrolyte and electrode.[66–68] Tafel slope is a good indicator of reaction kinetics and the rate-determining step of electrocatalytic reactions. The Sm-FeP@CC exhibits a much lower Tafel slope of 85.9 mV dec^{-1} than that of FeP@CC (184.3 mV dec^{-1}), which is close to commercial Pt/C (63.9 mV dec^{-1}), demonstrating the favorable HER kinetics *via* the Volmer–Heyrovsky route (Fig. 4(c)). Besides, such remarkable HER performance of Sm-FeP@CC surpasses that of most recently reported Fe-based catalysts in alkaline electrolyte, as listed in Fig. 4(d) and Table S1 (ESI†). The HER selectivity of Sm-FeP@CC was further studied by a sealed drainage gas collector system (Fig. S8, ESI†). As displayed in Fig. 4(e), the experimental H_2 yield of Sm-FeP@CC is close to the theoretical value and the faradaic efficiency is close to 100%, indicating the high HER selectivity. The Sm-FeP@CC also displays good electrocatalytic stability for the HER. As indicated in Fig. 4(f), the polarization curve after 3000 cyclic voltammetry (CV) cycles overlaps the initial one; while the current density barely changes after more than 40 hours of the *i*–*t* chronoamperometric test, which is better than that of FeP@CC (Fig. S9, ESI†). After the *i*–*t* test, the nanorod array structure and composition of Sm-FeP@CC are well maintained (Fig. S10 and S11, ESI†), which is probably the main reason for the excellent stability. The above electrocatalytic results confirm that Sm-FeP@CC is a highly active and stable HER electrocatalyst. To elucidate the superior HER activity of Sm-FeP@CC, the reactive active sites were studied through the electrochemical surface area (ECSA), which was calculated by the double-layer capacitance (C_{dl}). The CV curves at different scan rates in the non-faradaic region were provided in Fig. S12 (ESI†). In Fig. 4(g), the Sm-FeP@CC has a much larger C_{dl} value of 31.2 mF cm^{-2} than that of FeP@CC (22.7 mF cm^{-2}) and FeOOH@CC (4.78 mF cm^{-2}). Based on the obtained C_{dl} values (Fig. 4(g)), the ECSA of Sm-FeP@CC was calculated to be about 780 cm^{-2}, which is much higher than that of FeP@CC (567.5 cm^{-2}) and FeO(OH)@CC (119.5 cm^{-2}), demonstrating the significant improvement of ECSA after the phosphating and the Sm doping. The fast charge transport and high electron conductivity also contribute to the excellent HER performance of Sm-FeP@CC. The electrochemical impedance spectroscopy (EIS) Nyquist plots show that the charge transfer resistance (R_{ct}) for Sm-FeP@CC is smaller than that for FeP@CC and FeO(OH)@CC (Fig. 4(h)).

Theoretical analysis

Density functional theory (DFT) calculations were performed to measure the enhanced HER activity after the Sm modulation over FeP. For the slab model, we compared the surface formation energy of (010), (011), and (101). Afterward, the (011) surface was used for mechanism investigation due to its lowest surface formation energy according to our tested results. After the cleavage of FeP bulk into the (011) slab model, the projected density of states (PDOS) for Fe-3d donates a certain occupancy around the Fermi level (E_F), indicating the metallic behavior of FeP for electronic conductivity (Fig. 5(a)). After the introduction of Sm into FeP, the metallic behavior is still conserved and accordingly, the induced Sm exhibits the large occupancy of the valence 4f states below the E_F (Fig. 5(b)). However, such Sm-4f states exhibit the orphaned property, which can be attributed to the localized nature that is hard to participate in the chemical bonding, also noted as low covalency in the Sm–P bond. For the HER performance, we completely consider the splitting of the H–OH bond to produce the co-adsorption of *H and *OH and the consecutive H_2 formation (Fig. 5(d) and (e)). For the co-adsorption state on FeP, both the *H and *OH are bonded with surface Fe sites, where the adsorption of *OH leads to the obvious bonding states contributed by Fe-3d and O-2p (Fig. S13, ESI†), while for Sm-FeP, the lower contribution of Sm-4f for covalency leads to the limited orbital overlap between the Sm site and *OH, which can be confirmed by the promotion of O-2p states (around 2 eV in PDOS) from bonding states, equipping O-2p states as the labile property (Fig. 5(c)). Such a limited orbital overlap between the Sm site and *OH can decrease the adsorption of *OH, which is also confirmed by free energy calculation in Fig. 5(f). For FeP, the desorption of *OH step is a non-spontaneous process with a great step uphill, which is assigned as the potential-determining step (PDS) in the HER. When introducing Sm into FeP, the limited orbital overlap between Sm and *OH can greatly decrease the step downhill for the formation of *H + *OH, resulting in a thermodynamic spontaneous process for the desorption of *OH step for Sm-FeP. As a result, the PDS process for Sm-FeP was switched to the formation process of H_2. As a result, with the modulation effect of Sm into FeP for decreased co-adsorption of *H and *OH, the Sm-FeP delivers the facilitated formation of *H from the water splitting. For the consideration of hydrophilicity, the free energy of H_2O adsorption for Sm-FeP was calculated to be −3.05 eV (Fig. S14, ESI†), indicating the spontaneous coverage of H_2O molecules for good hydrophilicity of Sm-FeP.

Application exploration and universal adaptation

Based on the excellent HER catalytic activity of Sm-FeP@CC, we carried out the explorations of practical application and universal adaptation. A two-electrode OER‖HER electrolyzer was assembled to investigate a feasible catalyst candidate of Sm-FeP@CC for overall water splitting. The Sm-FeP@CC‖RuO_2 requires a cell voltage of 1.59 V to achieve a current density of 10 mA cm^{-2} (Fig. 6(a)), which exceeds FeP@CC. As the cell voltage increases, large amounts of hydrogen and oxygen escape from the surface of the carbon cloth, respectively (Fig. 6(a), inset). Besides, the current density increases sharply following the

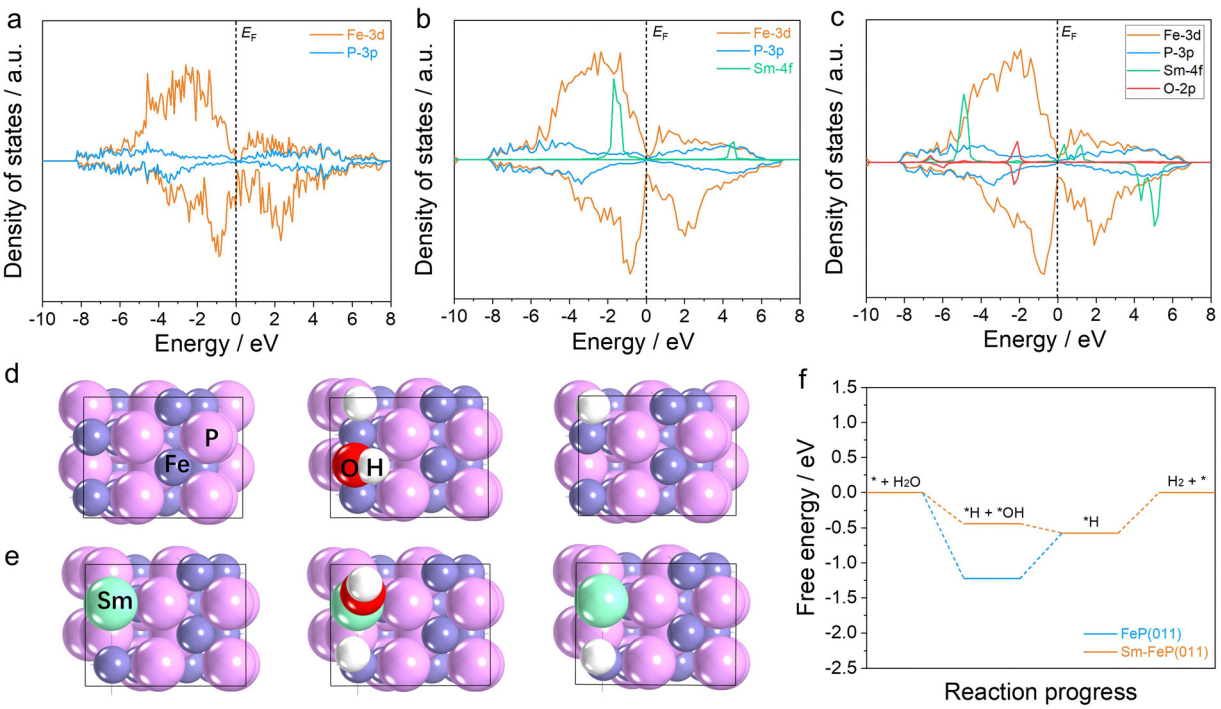

Fig. 5 (a) PDOS of Fe-3d and P-3p in FeP (011); (b) PDOS of Fe-3d, P-3p and Sm-4f in Sm-FeP (011); (c) PDOS of Fe-3d, P-3p, Sm-4f and O-2p in Sm-FeP (011) + (*H + *OH); geo-optimized model of (d) FeP and (e) Sm-FeP in the HER; and (f) Gibbs free energy diagram on the Sm-FeP(011) and FeP(011).

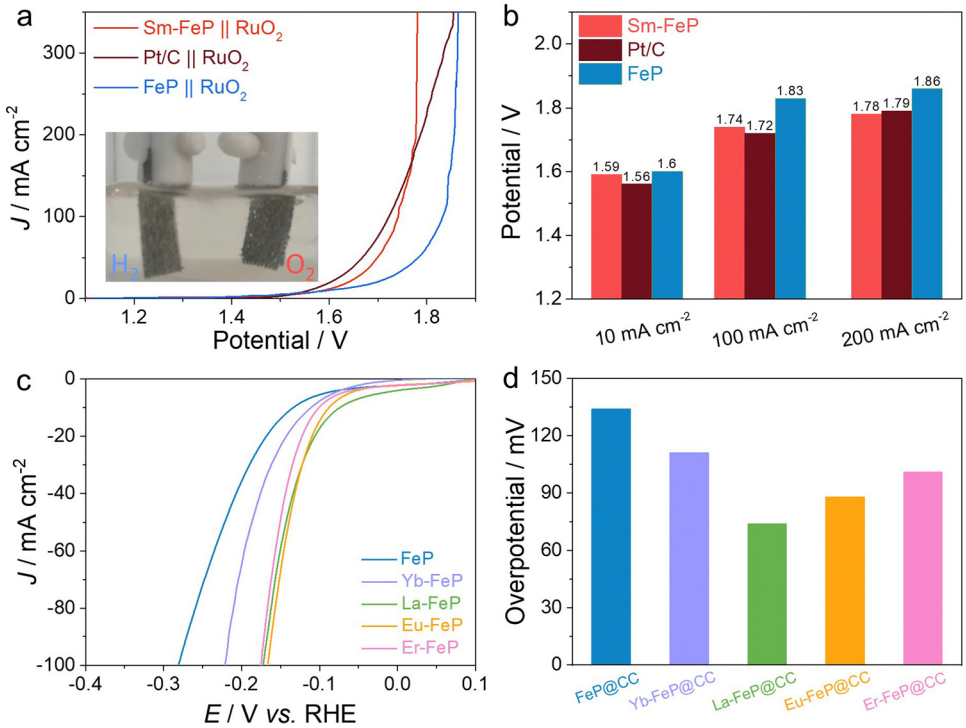

Fig. 6 (a) Polarization curves of Sm-FeP@CC‖Pt/C and other counterparts; inset: digital photograph of H_2 and O_2 bubbles during electrolysis; (b) cell voltage comparisons of Sm-FeP@CC‖Pt/C and other counterparts at current densities of 10, 100, and 200 mA cm^{-2}; (c) comparison of HER polarization curves of different RE-doped FeP@CC in 1 M KOH solution; and (d) overpotentials of different RE-doped FeP@CC at 10 mA cm^{-2}.

increase of the cell voltage for the Sm-FeP@CC‖RuO_2 (Fig. 6(b)), which leads to a low cell voltage of 1.74 and 1.78 V at 100 and 200 mA cm^{-2} respectively. The stability of overall water splitting on Sm-FeP@CC‖RuO_2 was evaluated by the *i–t* curve (Fig. S15, ESI†). As observed, the operating current density of Sm-FeP@CC‖RuO_2 shows a small attenuation up to 25 h, which is better than that of the FeP@CC‖RuO_2 electrolyzer, verifying that the HER activity of Sm-FeP@CC was well retained. To explore the universality of rare-earth-doped FeP for improving the HER, the FeP samples doped with different rare earths (such as Yb, Eu, La and Er) were prepared by a similar method as with Sm-FeP@CC. The successful doping of rare earths on carbon cloth-loaded FeP was confirmed by elemental mapping images (Fig. S16, ESI†), suggesting a universal synthesis strategy. Fig. 6(c) and (d) show that the HER activity of the catalysts after rare earth doping has been improved to varying degrees, implying that rare-earth-doped FeP is a promising class of HER catalyst.

Conclusions

In summary, a series of RE-doped FeP catalysts was synthesized through a universal plasma-assisted strategy for improving the HER performance. An Ar-plasma beam with high energy can shed the surface light atoms to form vacancies, which facilitates the doping of RE elements. Taking Sm-FeP as an example, it exhibits high electrocatalytic performance for the HER including a low overpotential, a small Tafel slope and good long-term stability, which exceeds the pure FeP catalyst. The as-assembled Sm-FeP@CC‖RuO_2 electrolyzer performs well in water splitting (1.59 V at 10 mA cm^{-2}). Theoretical calculations reveal that the increased HER performance on Sm-FeP is due to the weakened co-adsorption of *OH and *H that are contributed by the splitting of H_2O, where the labile O 2p state in *OH denotes the weak bonding at the Sm site. As a result, the formation of *H by removing the *OH is favored for the consecutive H_2 release. Finally, the plasma-assisted strategy proved to be useful for the synthesis of other RE-FeP (RE = Yb, Eu, La, and Er) catalysts in general, which also exhibited varying degrees of performance enhancement towards the HER.

Conflicts of interest

There are no conflicts to declare.

Acknowledgements

This work was financially supported by the National Natural Science Foundation of China (22109073, 22072067), the Natural Science Foundation of Jiangsu Province (BK20221321), Jiangsu Specially Appointed Professor Plan, and Science and Technology Innovation Project for Overseas Researchers in Nanjing. The authors are also grateful for support from the National and Local Joint Engineering Research Center of Biomedical Functional Materials and a project sponsored by the Priority

Academic Program Development of Jiangsu Higher Education Institutions.

References

1 G. Glenk and S. Reichelstein, Economics of converting renewable power to hydrogen, *Nat. Energy*, 2019, **4**, 216–222.
2 Q. Zhou, Z. Wang, H. Yuan, J. Wang and H. Hu, Rapid hydrogen adsorption–desorption at sulfur sites *via* an interstitial carbon strategy for efficient HER on MoS_2, *Appl. Catal., B*, 2023, **332**, 122750.
3 J. Zhang, R. Cui, C. Gao, L. Bian, Y. Pu, X. Zhu, X. A. Li and W. Huang, Cation-modulated HER and OER activities of hierarchical VOOH hollow architectures for high-efficiency and stable overall water splitting, *Small*, 2019, **15**, 1904688.
4 Y. Huang, M. Li, F. Pan, Z. Zhu, H. Sun, Y. Tang and G. Fu, Plasma-induced Mo-doped Co_3O_4 with enriched oxygen vacancies for electrocatalytic oxygen evolution in water splitting, *Carbon Energy*, 2022, **5**, e279.
5 D. Wang, X. Jiang, Z. Lin, X. Zeng, Y. Zhu, Y. Wang, M. Gong, Y. Tang and G. Fu, Ethanol-induced hydrogen insertion in ultrafine IrPdH boosts pH-universal hydrogen evolution, *Small*, 2022, **18**, 2204063.
6 S. Li, P. Ren, C. Yang, X. Liu, Z. Yin, W. Li, H. Yang, J. Li, X. Wang, Y. Wang, R. Cao, L. Lin, S. Yao, X. Wen and D. Ma, Fe_5C_2 nanoparticles as low-cost HER electrocatalyst: the importance of Co substitution, *Sci. Bull.*, 2018, **63**, 1358–1363.
7 W. Sheng, Z. Zhuang, M. Gao, J. Zheng, J. G. Chen and Y. Yan, Correlating hydrogen oxidation and evolution activity on platinum at different pH with measured hydrogen binding energy, *Nat. Commun.*, 2015, **6**, 5848.
8 B. Ren, J. Cao, H. Zhang, C. Han and W. Xu, Recent progress in the development of single-atom electrocatalysts for highly efficient hydrogen evolution reactions, *Mater. Chem. Front.*, 2023, DOI: **10.1039/D3QM00157A**.
9 Q. Dang, Y. Sun, X. Wang, W. Zhu, Y. Chen, F. Liao, H. Huang and M. Shao, Carbon dots-Pt modified polyaniline nanosheet grown on carbon cloth as stable and high-efficient electrocatalyst for hydrogen evolution in pH-universal electrolyte, *Appl. Catal., B*, 2019, **257**, 117905.
10 S. Anantharaj and S. Noda, Layered 2D PtX_2 (X = S, Se, Te) for the electrocatalytic HER in comparison with Mo/WX_2 and Pt/C: are we missing the bigger picture?, *Energy Environ. Sci.*, 2022, **15**, 1461–1478.
11 S. Anantharaj, P. E. Karthik, B. Subramanian and S. Kundu, Pt nanoparticle anchored molecular self-assemblies of DNA: an extremely stable and efficient HER electrocatalyst with ultralow Pt content, *ACS Catal.*, 2016, **6**, 4660–4672.
12 Y. Guo, B. Hou, X. Cui, X. Liu, X. Tong and N. Yang, Pt Atomic layers loosted hydrogen evolution reaction in non-acidic media, *Adv. Energy Mater.*, 2022, **12**, 2201548.
13 X. Lu, X. Tan, Q. Zhang, R. Daiyan, J. Pan, R. Chen, H. A. Tahini, D.-W. Wang, S. C. Smith and R. Amal, Versatile electrocatalytic processes realized by Ni, Co and Fe alloyed core coordinated carbon shells, *J. Mater. Chem. A*, 2019, **7**, 12154–12165.
14 Y. Gu, B. Wei, D. Legut, Z. Fu, S. Du, H. Zhang, J. S. Francisco and R. Zhang, Single atom-modified hybrid transition metal carbides as efficient hydrogen evolution reaction catalysts, *Adv. Funct. Mater.*, 2021, **31**, 2104285.
15 D. Jin, F. Qiao, H. Chu and Y. Xie, Progress in electrocatalytic hydrogen evolution of transition metal alloys: synthesis, structure, and mechanism analysis, *Nanoscale*, 2023, **15**, 7202.
16 W. Du, Y. Shi, W. Zhou, Y. Yu and B. Zhang, Unveiling the in situ dissolution and polymerization of Mo in Ni_4Mo alloy for promoting the hydrogen evolution reaction, *Angew. Chem., Int. Ed.*, 2021, **60**, 7051–7055.
17 Z. Zhu, H. Yin, C.-T. He, M. Al-Mamun, P. Liu, L. Jiang, Y. Zhao, Y. Wang, H.-G. Yang, Z. Tang, D. Wang, X.-M. Chen and H. Zhao, Ultrathin transition metal dichalcogenide/3d metal hydroxide hybridized nanosheets toenhance hydrogen evolution activity, *Adv. Mater.*, 2018, **30**, 1801171.
18 Y. Zhu, X. Wang, X. Zhu, Z. Wu, D. Zhao, F. Wang, D. Sun, Y. Tang, H. Li and G. Fu, Improving the oxygen evolution activity of layered double-hydroxide *via* erbium-induced electronic engineering, *Small*, 2023, **19**, 2206531.
19 D. Tian, S. R. Denny, K. Li, H. Wang, S. Kattel and J. G. Chen, Density functional theory studies of transition metal carbides and nitrides as electrocatalysts, *Chem. Soc. Rev.*, 2021, **50**, 12338–12376.
20 J. Li, M. Song, Y. Hu, Y. Zhu, J. Zhang and D. Wang, Hybrid heterostructure Ni_3N|NiFeP/FF self-supporting electrode for high-current-density alkaline water electrolysis, *Small Methods*, 2023, **7**, 2201616.
21 Y. Zhang, J. Yang, Z. Yu, Y. Hou, R. Jiang, J. Huang, F. Yang, S. Yao, L. Gao and W. Tang, Modulating carbon-supported transition metal oxide by electron-giving and electron-absorbing functional groups towards efficient overall water splitting, *Chem. Eng. J.*, 2021, **416**, 129124.
22 X.-F. Lu, L.-F. Gu, J.-W. Wang, J.-X. Wu, P.-Q. Liao and G.-R. Li, Bimetal-organic framework derived $CoFe_2O_4$/C porous hybrid nanorod arrays as high-performance electrocatalysts for oxygen evolution reaction, *Adv. Mater.*, 2017, **29**, 1604437.
23 K. Liu, Z. Zhu, M. Jiang, L. Li, L. Ding, M. Li, D. Sun, G. Yang, G. Fu and Y. Tang, Boosting electrocatalytic oxygen evolution over Ce-Co_9S_8 core-shell nanoneedle arrays by electronic and architectural dual engineering, *Chem. – Eur. J.*, 2022, **28**, e202200664.
24 Y. Guo, T. Park, J. W. Yi, J. Henzie, J. Kim, Z. Wang, B. Jiang, Y. Bando, Y. Sugahara, J. Tang and Y. Yamauchi, Nanoarchitectonics for transition-metal-sulfide-based electrocatalysts for water splitting, *Adv. Mater.*, 2019, **31**, 1807134.
25 J. Su, J. Zhou, L. Wang, C. Liu and Y. Chen, Synthesis and application of transition metal phosphides as electrocatalyst for water splitting, *Sci. Bull.*, 2017, **62**, 633–644.
26 A. Parra-Puerto, K. L. Ng, K. Fahy, A. E. Goode, M. P. Ryan and A. Kucernak, Supported transition metal phosphides: activity survey for HER, ORR, OER, and corrosion resistance

in acid and alkaline electrolytes, *ACS Catal.*, 2019, **9**, 11515–11529.

27 H. J. Pei, L. M. Zhang, G. Zhi, D. Z. Kong, Y. Wang, S. Z. Huang, J. H. Zang, T. T. Xu, H. Wang and X. J. Li, Rational construction of hierarchical porous FeP nanorod arrays encapsulated in polypyrrole for efficient and durable hydrogen evolution reaction, *Chem. Eng. J.*, 2022, **433**, 133643.

28 P. Jiang, Q. Liu, Y. H. Liang, J. Q. Tian, A. M. Asiri and X. P. Sun, A cost-effective 3D hydrogen evolution cathode with high catalytic activity: FeP nanowire array as the active phase, *Angew. Chem., Int. Ed.*, 2014, **53**, 12855–12859.

29 Y. Shi and B. Zhang, Recent advances in transition metal phosphide nanomaterials: synthesis and applications in hydrogen evolution reaction, *Chem. Soc. Rev.*, 2016, **45**, 1529–1541.

30 J. Q. Zhang, X. Shang, H. Ren, J. Q. Chi, H. Fu, B. Dong, C. G. Liu and Y. M. Chai, Modulation of inverse spinel Fe_3O_4 by phosphorus doping as an industrially promising electrocatalyst for hydrogen evolution, *Adv. Mater.*, 2020, **32**, 1907792.

31 Y. D. Yao, N. Mahmood, L. Pan, G. Q. Shen, R. R. Zhang, R. J. Gao, F. E. Aleem, X. Y. Yuan, X. W. Zhang and J. J. Zou, Iron phosphide encapsulated in P-doped graphitic carbon as efficient and stable electrocatalyst for hydrogen and oxygen evolution reactions, *Nanoscale*, 2018, **10**, 21327–21334.

32 X. J. Zhai, Q. P. Yu, G. S. Liu, J. L. Bi, Y. Zhang, J. Q. Chi, J. P. Lai, B. Yang and L. Wang, Hierarchical microsphere MOF arrays with ultralow Ir doping for efficient hydrogen evolution coupled with hydrazine oxidation in seawater, *J. Mater. Chem. A*, 2021, **9**, 27424–27433.

33 S. Zhu, L. Yang, J. Bai, Y. Chu, J. Liu, Z. Jin, C. Liu, J. Ge and W. Xing, Ultra-stable Pt_5La intermetallic compound towards highly efficient oxygen reduction reaction, *Nano Res.*, 2023, **16**, 2035–2040.

34 X. Wei, Y. Liu, X. Zhu, S. Bo, L. Xiao, C. Chen, T. T. T. Nga, Y. He, M. Qiu, C. Xie, D. Wang, Q. Liu, F. Dong, C.-L. Dong, X.-Z. Fu and S. Wang, Dynamic reconstitution between copper single atoms and clusters for electrocatalytic urea synthesis, *Adv. Mater.*, 2023, 2300020.

35 X. Peng, Y. Mi, H. Bao, Y. Liu, D. Qi, Y. Qiu, L. Zhuo, S. Zhao, J. Sun, X. Tang, J. Luo and X. Liu, Ambient electrosynthesis of ammonia with efficient denitration, *Nano Energy*, 2020, **78**, 105321.

36 X. Wang, J. Wang, P. Wang, L. Li, X. Zhang, D. Sun, Y. Li, Y. Tang, Y. Wang and G. Fu, Engineering 3d–2p–4f gradient orbital coupling to enhance electrocatalytic oxygen reduction, *Adv. Mater.*, 2022, **34**, 2206540.

37 M. Li, Y. Wang, Y. Zheng, G. Fu, D. Sun, Y. Li, Y. Tang and T. Ma, Gadolinium-induced valence structure engineering for enhanced oxygen electrocatalysis, *Adv. Energy Mater.*, 2020, **10**, 1903833.

38 W. Peng, X. G. Li, Z. M. He, Z. S. Li, X. Y. Zhang, X. P. Sun, Q. Li, H. Yang, J. T. Han and Y. H. Huang, Electron density modulation of MoP by rare earth metal as highly efficient electrocatalysts for pH-universal hydrogen evolution reaction, *Appl. Catal., B*, 2021, **299**, 120657.

39 M. Li, X. Wang, K. Liu, H. Sun, D. Sun, K. Huang, Y. Tang, W. Xing, H. Li and G. Fu, Reinforce the Co–O covalency *via* Ce(4f)–O(2p)–Co(3d) gradient orbital coupling for high-efficiency oxygen evolution, *Adv. Mater.*, 2023, DOI: **10.1002/adma.202302462**.

40 L. Yin, S. Zhang, M. Sun, S. Wang, B. Huang and Y. Du, Heteroatom-driven coordination fields altering single cerium atom sites for efficient oxygen reduction reaction, *Adv. Mater.*, 2023, DOI: **10.1002/adma.202302485**.

41 Z. Liang, L. Yin, H. Yin, Z. Yin and Y. Du, Rare earth element based single-atom catalysts: synthesis, characterization and applications in photo/electro-catalytic reactions, *Nanoscale Horiz.*, 2022, **7**, 31–40.

42 S. Meng, G. Li, P. Wang, M. He, X. Sun and Z. Li, Rare earth-based MOFs for photo/electrocatalysis, *Mater. Chem. Front.*, 2023, **7**, 806–827.

43 X. Wang, Y. Zhu, H. Li, J.-M. Lee, Y. Tang and G. Fu, Rare-earth single-atom catalysts: a new frontier in photo/electrocatalysis, *Small Methods*, 2022, **6**, 2200413.

44 X. Wang, Y. Tang, J.-M. Lee and G. Fu, Recent advances in rare-earth-based materials for electrocatalysis, *Chem. Catal.*, 2022, **2**, 967–1008.

45 H. Sun, Z. Yan, C. Tian, C. Li, X. Feng, R. Huang, Y. Lan, J. Chen, C.-P. Li, Z. Zhang and M. Du, Bixbyite-type Ln_2O_3 as promoters of metallic Ni for alkaline electrocatalytic hydrogen evolution, *Nat. Commun.*, 2022, **13**, 3857.

46 F. Li, M. Jiang, C. Lai, H. Xu, K. Zhang and Z. Jin, Yttrium- and cerium-codoped ultrathin metal–organic framework nanosheet arrays for high-efficiency electrocatalytic overall water splitting, *Nano Lett.*, 2022, **22**, 7238–7245.

47 F. Gong, S. Ye, M. Liu, J. Zhang, L. Gong, G. Zeng, E. Meng, P. Su, K. Xie, Y. Zhang and J. Liu, Boosting electrochemical oxygen evolution over yolk-shell structured O–MoS_2 nanoreactors with sulfur vacancy and decorated Pt nanoparticles, *Nano Energy*, 2020, **78**, 105284.

48 J. Wan, W. Chen, C. Jia, L. Zheng, J. Dong, X. Zheng, Y. Wang, W. Yan, C. Chen, Q. Peng, D. Wang and Y. Li, Defect effects on TiO_2 nanosheets: stabilizing single atomic site au and promoting catalytic properties, *Adv. Mater.*, 2018, **30**, 1705369.

49 I. Kumar and A. K. Gathania, Photoluminescence and quenching study of the Sm^{3+}-doped $LiBaPO_4$ phosphor, *J. Mater. Sci.: Mater. Electron.*, 2022, **33**, 328–341.

50 Z. Li, X. Wu, X. Jiang, B. Shen, Z. Teng, D. Sun, G. Fu and Y. Tang, Surface carbon layer controllable Ni_3Fe particles confined in hierarchical N-doped carbon framework boosting oxygen evolution reaction, *Adv. Powder Mater.*, 2022, **1**, 100020.

51 T. Li, Y. Hu, K. Liu, J. Yin, Y. Li, G. Fu, Y. Zhang and Y. Tang, Hollow yolk-shell nanoboxes assembled by Fe-doped Mn_3O_4 nanosheets for high-efficiency electrocatalytic oxygen reduction in Zn–Air battery, *Chem. Eng. J.*, 2022, **427**, 131992.

52 Y. Deng, X. Xi, Y. Xia, Y. Cao, S. Xue, S. Wan, A. Dong and D. Yang, 2D FeP nanoframe superlattices *via* space-confined topochemical transformation, *Adv. Mater.*, 2022, **34**, 2109145.

53 M. Wang, Y. Tuo, X. Li, Q. Hua, F. Du and L. Jiang, Mesoporous Mn-doped FeP: facile synthesis and enhanced electrocatalytic activity for hydrogen evolution in a wide ph range, *ACS Sustainable Chem. Eng.*, 2019, **7**, 12419–12427.

54 X. Zhao, Z. Zhang, X. Cao, J. Hu, X. Wu, A. Y. R. Ng, G.-P. Lu and Z. Chen, Elucidating the sources of activity and stability of FeP electrocatalyst for hydrogen evolution reactions in acidic and alkaline media, *Appl. Catal., B*, 2020, **260**, 118156.

55 Y. X. Luo, W. B. Qiu, R. P. Liang, X. H. Xia and J. D. Qiu, Mo-doped FeP nanospheres for artificial nitrogen fixation, *ACS Appl. Mater. Interfaces*, 2020, **12**, 17452–17458.

56 W. Zhong, C. Yang, J. Wu, W. Xu, R. Zhao, H. Xiang, K. Shen and X. Li, Adsorption site engineering: Cu–$Ni(OH)_2$ sheets for efficient hydrogen evolution, *J. Mater. Chem. A*, 2021, **9**, 17521–17527.

57 G. Zhou, S. Zhang, Y. Zhu, J. Li, K. Sun, H. Pang, M. Zhang, Y. Tang and L. Xu, Manipulating the rectifying contact between ultrafine Ru nanoclusters and N-Doped carbon nanofibers for high-efficiency ph-universal electrocatalytic hydrogen evolution, *Small*, 2023, **19**, 2206781.

58 Y. Liu, Q. Feng, W. Liu, Q. Li, Y. Wang, B. Liu, L. Zheng, W. Wang, L. Huang, L. Chen, X. Xiong and Y. Lei, Boosting interfacial charge transfer for alkaline hydrogen evolution *via* rational interior Se modification, *Nano Energy*, 2021, **81**, 105641.

59 Z. Wu, D. Nie, M. Song, T. Jiao, G. Fu and X. Liu, Facile synthesis of Co–Fe–B–P nanochains as an efficient bifunctional electrocatalysts for overall water-splitting, *Nanoscale*, 2019, **11**, 7506–7512.

60 M. Song, Z. Zhang, Q. Li, W. Jin, Z. Wu, G. Fu and X. Liu, Ni-foam supported Co(OH)F and Co–P nanoarrays for energy-efficient hydrogen production *via* urea electrolysis, *J. Mater. Chem. A*, 2019, **7**, 3697–3703.

61 Y. Zhang, L. Gao, E. J. M. Hensen and J. P. Hofmann, Evaluating the stability of Co_2P electrocatalysts in the hydrogen evolution reaction for both acidic and alkaline electrolytes, *ACS Energy Lett.*, 2018, **3**, 1360–1365.

62 S. Liu, J. Zhu, M. Sun, Z. Ma, K. Hu, T. Nakajima, X. Liu, P. Schmuki and L. Wang, Promoting the hydrogen evolution reaction through oxygen vacancies and phase transformation engineering on layered double hydroxide nanosheets, *J. Mater. Chem. A*, 2020, **8**, 2490–2497.

63 Y. Ren, X. Lei, H. Wang, J. Xiao and Z. Qu, Enhanced Catalytic Performance of La-doped $CoMn_2O_4$ catalysts by regulating oxygen species activity for VOCs oxidation, *ACS Catal.*, 2023, **13**, 8293–8306.

64 Y. Li, J. Liu, X. Chen, J. Wu, N. Li, W. He and Y. Feng, T Tailoring surface properties of electrodes for synchronous enhanced extracellular electron transfer and enriched exoelectrogens in microbial fuel cells, *ACS Appl. Mater. Interfaces*, 2021, **13**, 58508–58521.

65 Z. Zhao, W. Jin, L. Xu, C. Wang, Y. Zhang and Z. Wu, Ultrafine Ir nanoparticles decorated on FeP/FeOOH with abundant interfaces *via* a facile corrosive approach for alkaline water-splitting, *J. Mater. Chem. A*, 2021, **9**, 12074–12079.

66 L. Zhang, J. Zhang, J. Fang, X.-Y. Wang, L. Yin, W. Zhu and Z. Zhuang, Cr-doped CoP nanorod arrays as high-performance hydrogen evolution reaction catalysts at high current density, *Small*, 2021, **17**, 2100832.

67 Y. Tan, R. Xie, S. Zhao, X. Lu, L. Liu, F. Zhao, C. Li, H. Jiang, G. Chai, D. J. L. Brett, P. R. Shearing, G. He and I. P. Parkin, Facile fabrication of robust hydrogen evolution electrodes under high current densities *via* Pt@Cu interactions, *Adv. Funct. Mater.*, 2021, **31**, 2105579.

68 B. Geng, F. Yan, L. Liu, C. Zhu, B. Li and Y. Chen, Ni/MoC heteronanoparticles encapsulated within nitrogen-doped carbon nanotube arrays as highly efficient self-supported electrodes for overall water splitting, *Chem. Eng. J.*, 2021, **406**, 126815.